



| | |
|-------------------------|--|
| Title | Infrared Spectra of Isomers of Protonated Aniline in Solid para-Hydrogen |
| Author(s) | Tsuge, Masashi; Chen, Yu-Hsuan; Lee, Yuan-Pern |
| Citation | Journal of Physical Chemistry A, 124(11), 2253-2263 https://doi.org/10.1021/acs.jpca.0c00241 |
| Issue Date | 2020-02-25 |
| Doc URL | http://hdl.handle.net/2115/80539 |
| Rights | This document is the Accepted Manuscript version of a Published Work that appeared in final form in The Journal of Physical Chemistry A, copyright c American Chemical Society after peer review and technical editing by the publisher. To access the final edited and published work see https://pubs.acs.org/doi/10.1021/acs.jpca.0c00241 . |
| Type | article (author version) |
| File Information | Journal of Physical Chemistry A_124_11.pdf |



[Instructions for use](#)

Infrared Spectra of Isomers of Protonated Aniline in Solid *para*-Hydrogen

Masashi Tsuge,^{*,†,‡} Yu-Hsuan Chen,[†] and Yuan-Pern Lee^{*,†,§,⊥}

[†]Department of Applied Chemistry and Institute of Molecular Science, National Chiao Tung University, Hsinchu 30010, Taiwan

[‡]Institute of Low Temperature Sciences, Hokkaido University, Sapporo 060-0819, Japan

[§]Center for Emergent Functional Matter Science, National Chiao Tung University, Hsinchu 30010, Taiwan

[⊥]Institute of Atomic and Molecular Sciences, Academia Sinica, Taipei 10617, Taiwan

ABSTRACT: The protonation sites of aniline molecule play important roles in its chemical reactions, but the preferred protonation site of gaseous aniline has yet to be determined. In this work, we recorded infrared (IR) absorption spectra of three isomers of protonated aniline, $\text{H}^+\text{C}_6\text{H}_5\text{NH}_2$, produced on electron bombardment during matrix deposition at 3.2 K of a mixture of aniline and *para*- H_2 . The intensities of IR lines of $\text{H}^+\text{C}_6\text{H}_5\text{NH}_2$ decreased during maintenance of the electron-bombarded matrix in darkness because of neutralization with electrons that were slowly released from their trapping sites. The observed lines were classified into three groups according to their behavior upon secondary photolysis with light at 375 and 254 nm and assigned to *para*-, *amino*-, and *ortho*- $\text{H}^+\text{C}_6\text{H}_5\text{NH}_2$, the three most stable isomers of protonated aniline, according to comparison of experimental spectra with quantum-chemically predicted spectra of five possible isomers of $\text{H}^+\text{C}_6\text{H}_5\text{NH}_2$. The spectra of *para*- and *ortho*- $\text{H}^+\text{C}_6\text{H}_5\text{NH}_2$ are newly distinguished. The approximate relative abundance of these isomers in solid *p*- H_2 was *para* : *amino* : *ortho* $\approx (1.0 \pm 0.1) : (1.0 \pm 0.6) : (0.6 \pm 0.1)$. The possible mechanisms of formation are discussed.

1. INTRODUCTION

The protonation of chemical species is important in many branches of physical science because a proton facilitates acid-base chemistry.¹ Protonated aromatic molecules play critical roles in many chemical and biological phenomena.²⁻⁴ For example, the electrophilic aromatic substitution reaction of benzene (C_6H_6) proceeds via $C_6H_6 + E^+ \rightleftharpoons [C_6H_6E]^+ \rightarrow C_6H_5E + H^+$, in which E^+ is an electrophile; $[C_6H_6E]^+$ can be regarded as a protonated substituted benzene.⁵⁻⁶ The preferred site of protonation in the substituted benzenes and the energetics of protonation are thus important in determining the rate of such chemical reactions. The physical conditions (e.g., temperature and pressure), the substitution by functional groups, and solvation might affect the preferential site of protonation. Spectral studies of isolated protonated aromatic species consequently provide insights to the intrinsic preference of the protonation sites.

Aniline ($C_6H_5NH_2$) is the simplest aromatic amine, in which one hydrogen is substituted with an amino group (NH_2). As shown in Figure 1, aniline has five distinct protonation sites, namely *para*-, *meta*-, *ortho*-, *ipso*-, and *amino*-positions; hereafter we designate the protonated aniline as $H^+C_6H_5NH_2$. The proton prefers to attach to the *amino*-position in aqueous solutions because of the stabilization by solvation,⁷⁻⁸ but the preferred sites of protonation in the gaseous phase are still uncertain according to numerous theoretical and experimental studies.⁹⁻²³

The most stable $H^+C_6H_5NH_2$ was predicted to be either *para*- or *amino*- $H^+C_6H_5NH_2$ depending on the method of quantum-chemical calculation.^{10-11, 16-20} From systematic high-level computations, Russo et al. reported that *para*- $H^+C_6H_5NH_2$ has the least energy, but the energy difference between *para*- and *amino*- $H^+C_6H_5NH_2$ is within 3 kJ mol^{-1} so that these isomers probably coexist.¹⁸ The G2MP2 and B3LYP methods with the triple-zeta basis sets give proton affinities similar to the experimental values, $874\text{--}877 \text{ kJ mol}^{-1}$.²⁴⁻²⁵

Mass-spectrometric experiments indicated that both *para*- and *amino*- $H^+C_6H_5NH_2$ are present in the gaseous phase but that their relative abundance depends strongly on the method

of production (ionization) and possibly the method of detection. According to Nold et al., the fast-atom bombardment (FAB) produces predominantly *amino*-H⁺C₆H₅NH₂, whereas the chemical ionization induces mixed protonation with the ring-protonated species predominating.¹⁵ In chemical ionization by H⁺, CH₃⁺, or C₂H₅⁺ ions, Wood et al. suggested that *para*-H⁺C₆H₅NH₂ is the predominant species according to their MS/MS measurements with collision-induced dissociation (CID).²⁶ In experiments with charge stripping followed by CID, Pachuta et al. identified that protonation occurs on the carbon ring,¹² consistent with the conclusion by Wood et al. In contrast, Smith et al. reported the predominant formation of *amino*-H⁺C₆H₅NH₂ from chemical ionization with CH₅⁺/CD₅⁺.¹⁴

The electrospray ionization (ESI) has also been utilized to study protonation of aniline.^{13, 22-}
²³ These experiments indicated that both the solvent used in ESI and the post-ESI source conditions greatly affect the ratio between *para*- and *amino*-H⁺C₆H₅NH₂. For example, Walker et al. demonstrated that ~96 % of *amino*-H⁺C₆H₅NH₂ and a minor proportion of *para*-H⁺C₆H₅NH₂ were produced in their ESI experiments; the proportion of *para*-H⁺C₆H₅NH₂ was significantly decreased when a protic solvent (methanol or water) was employed, compared to the use of an aprotic solvent (acetonitrile).²³ When clustered with solvent molecules, *para*-H⁺C₆H₅NH₂ can be converted to *amino*-H⁺C₆H₅NH₂ but not vice versa, indicating that, in ESI experiments, ion structures might be altered before mass-spectrometric characterization. Although challenging, non-perturbative formation and definitive spectral detection of these protonated isomers is hence desirable to provide more accurate relative populations among varied sites of protonation.

Dopfer and co-workers conducted infrared photodissociation (IRPD) spectroscopy on H⁺C₆H₅NH₂ tagged with Ar or N₂; the H⁺C₆H₅NH₂ isomers were accumulated in an ion trap and IRPD spectra in the NH-stretching region were recorded. These authors reported the observation of lines in two groups that are assignable to *amino*-H⁺C₆H₅NH₂ and *ortho*- and/or

para-H⁺C₆H₅NH₂ according to the variation of the spectra depending on the ligands, dissociation pattern, and a comparison with theoretical predictions;²⁰ the infrared (IR) spectra of *ortho*- and *para*-H⁺C₆H₅NH₂ were predicted to be similar in the NH-stretching region. Obtaining spectra with improved spectral resolution and in fingerprint regions is hence critical to distinguish these isomers unambiguously.

Our method to produce protonated species in solid *para*-hydrogen (*p*-H₂) by electron bombardment has several advantages to solve the problems discussed above.²⁷⁻²⁸ The IR spectra of protonated species obtained in this method exhibit narrow lines, true relative IR intensities, and a wide spectral coverage, suitable to distinguish the spectra of *ortho*- and *para*-H⁺C₆H₅NH₂. Although this method lacks mass selection, the electron bombardment of a *p*-H₂ matrix containing aromatic species has been proven to produce protonated and hydrogenated species with negligible fragmentations; methods to distinguish protonated and hydrogenated products have been established.²⁹⁻³⁶ Because the spectral shift from the gaseous phase is expected to be small in solid *p*-H₂, a comparison with quantum-chemically predicted IR spectra of potential carriers provides definitive assignments of these species. In this work, we applied this method to identify unambiguously the IR spectra of *para*-, *ortho*-, and *amino*-H⁺C₆H₅NH₂.

2. METHODS

The experimental setup for *p*-H₂ matrix-isolation IR spectroscopy, combined with electron bombardment during matrix deposition, is described elsewhere.²⁹ A gaseous mixture was deposited onto a gold-plated copper substrate that also reflects the incident IR beam to the detector for reflective absorption measurements in spectral range 5000–450 cm⁻¹. Infrared absorption spectra were recorded with a Fourier-transform infrared (FTIR) spectrometer equipped with a KBr beam splitter and a HgCdTe detector cooled to 77 K with liquid nitrogen. Two hundred scans at resolution 0.25 cm⁻¹ were recorded at each stage of the experiment.

A gaseous mixture of C₆H₅NH₂/*p*-H₂ (prepared in a glass bulb with an estimated mixing ratio ~70 ppm) was bombarded with electrons during deposition at 3.2 K at a flow rate of 13 mmol h⁻¹ over a period of 8–10 h. An electron beam of kinetic energy 200 eV and current 30 μA was provided from an electron gun. The deposited matrix was maintained in darkness for a prolonged period to distinguish cationic and neutral species. Secondary photolysis was subsequently performed using light at 375 ± 10 nm from a light-emitting diode and light at 254 nm from a low-pressure Hg lamp to further differentiate various species.

Pure *p*-H₂ was prepared on catalytic conversion of *normal*-H₂ (*n*-H₂) at low temperatures; *n*-H₂ was introduced into a copper cell filled with a catalyst (iron(III)-oxide hydrated, 30–50 mesh, Aldrich) and maintained at 12–13 K with a closed-cycle helium refrigerator. The resultant *p*-H₂ typically contained *ortho*-H₂ at less than 100 ppm. The aniline was obtained commercially (≥99.5 %, Aldrich) and degassed with several freeze-pump-thaw cycles.

The mixing ratios of products in solid *p*-H₂ were estimated using the method developed by Tam and Fajardo.³⁷⁻³⁸ According to their method, the mixing ratio *x* (in ppm) in solid *p*-H₂ is estimated as

$$x = \frac{2.303 \int \log_{10}(I/I_0)dv}{\epsilon l} \times V_m \times 10^6, \quad (1)$$

in which ϵ is the absorption coefficient in cm mol⁻¹, $\int \log_{10}(I/I_0)dv$ is the observed integrated absorbance, l (in cm) is the length of the IR absorption path through solid *p*-H₂, and V_m (= 23.16 cm³ mol⁻¹) is the molar volume of solid *p*-H₂. Infrared intensities calculated with the B3LYP/ cc-pVTZ method were used for ϵ . Length l of the IR path was estimated from the integrated band area of transition S₁(0) + S₀(0) of the *p*-H₂ matrix.³⁹⁻⁴⁰

Quantum-chemical calculations were performed with programs Gaussian 09 (Rev. E.01)⁴¹ and Gaussian 16 (Rev. B.01).⁴² The density-functional theory with B3LYP functionals⁴³⁻⁴⁴ and Dunning's correlation-consistent basis set, cc-pVTZ,⁴⁵ were employed to perform geometry optimization and harmonic vibrational analysis. Scaling factors for harmonic vibrational

wavenumbers were obtained on comparing wavenumbers observed for C₆H₅NH₂ in solid *p*-H₂ with those predicted; see Sec. 4A for details. In addition, anharmonic vibrational wavenumbers were calculated with a second-order vibrational perturbation theory (VPT2),⁴⁶ implemented in Gaussian 09. For the comparison of single point energies, the zero-point vibrational energy (ZPVE) was corrected using harmonic wavenumbers without scaling.

3. COMPUTATIONAL RESULTS

Figure 2 shows the geometries of aniline and five possible isomers of protonated aniline, *para*-, *meta*-, *ortho*-, *ipso*-, and *amino*-H⁺C₆H₅NH₂, optimized with the B3LYP/cc-pVTZ method; representative bond lengths and angles are presented. Protonation at the benzene ring distorts the ring slightly as indicated by bond angles less than 120°, but the carbon atoms remain in one plane except for the *ipso*-H⁺C₆H₅NH₂ isomer. The C1–N bonds in *para*-, *ortho*-, and *meta*-isomers are shortened from that of aniline (1.395 Å according to the B3LYP/cc-pVTZ method) and those in *amino*- and *ipso*-isomers are lengthened, indicating that protonation affects the resonance pattern of π -electrons; i.e., the double-bond character of the C1–N bond of aniline is enhanced in *para*-, *ortho*-, and *meta*-isomers and diminished in other isomers.

Among these possible protonated-isomers, *para*-H⁺C₆H₅NH₂ has the least energy. The *amino*- and *ortho*-H⁺C₆H₅NH₂ isomers have energies greater by 7.8 and 18.4 kJ mol⁻¹, respectively, than that of *para*-H⁺C₆H₅NH₂; all energies are corrected for ZPVE. The energies of *meta*- and *ipso*-H⁺C₆H₅NH₂ are much greater (+96.0 and +168.3 kJ mol⁻¹, respectively). A potential-energy diagram for the protonation of aniline and the isomerization of protonated aniline is presented in Figure 3 and summarized in Table 1. As compared in Table 1, the order of the two most stable isomers differs between our work and that calculated with the B3LYP/6-311G(2df,2pd) method by Pasker et al.²⁰ We also calculated the energies of these isomers with the B3LYP/6-311G(2df,2pd) method and found discrepancies between our results and those of

Pasker et al., as compared in Table 1; the literature values might be in error. The proton-transfer reactions from H_3^+ to aniline, $\text{C}_6\text{H}_5\text{NH}_2 + \text{H}_3^+ \rightarrow \text{H}^+\text{C}_6\text{H}_5\text{NH}_2 + \text{H}_2$, have no barrier, with exothermicity ranging from 305.9 kJ mol⁻¹ for the formation of *ipso*- $\text{H}^+\text{C}_6\text{H}_5\text{NH}_2$ to 474.3 kJ mol⁻¹ for the formation of *para*- $\text{H}^+\text{C}_6\text{H}_5\text{NH}_2$. Although the barriers for isomerization from one site to a neighboring site via TS1–TS4 are smaller than the exothermicity of the protonation reactions, once a product is stabilized, thermal isomerization to other isomers is unlikely at low temperatures except for *ipso*- $\text{H}^+\text{C}_6\text{H}_5\text{NH}_2$, which might spontaneously isomerize to *ortho*- $\text{H}^+\text{C}_6\text{H}_5\text{NH}_2$.

Vibrational wavenumbers and IR intensities of the representative vibrational modes of *para*-, *ortho*-, and *amino*- $\text{H}^+\text{C}_6\text{H}_5\text{NH}_2$, predicted with the B3LYP/cc-pVTZ method, are listed in Tables 2, 3, and 4, respectively; the full lists are available in Tables S-1–S-3. Those predicted for *meta*- and *ipso*- $\text{H}^+\text{C}_6\text{H}_5\text{NH}_2$ are listed in Tables S-4 and S-5, respectively. For protonated aniline, the vibrational lines associated with the NH_2 (or NH_3) group are intense and characteristic. For *para*- $\text{H}^+\text{C}_6\text{H}_5\text{NH}_2$, the NH_2 -stretching modes are predicted at 3510 (ν_{28}) and 3407 (ν_1) cm⁻¹, and the NH_2 -scissoring mode at 1661 (ν_5) cm⁻¹; similar wavenumbers are predicted for *ortho*- $\text{H}^+\text{C}_6\text{H}_5\text{NH}_2$. For *amino*- $\text{H}^+\text{C}_6\text{H}_5\text{NH}_2$, the NH -stretching modes are predicted at 3336 (ν_1), 3311 (ν_{27}), and 3255 (ν_2) cm⁻¹, and the NH_3 umbrella mode at 1470 (ν_{13}) cm⁻¹. Another group of relatively intense vibrational lines is associated with the CH_2 group; these include the CH_2 -scissoring mode of *para*- $\text{H}^+\text{C}_6\text{H}_5\text{NH}_2$ at 1338 (ν_{32}) cm⁻¹, the CH_2 -scissoring and wagging modes of *ortho*- $\text{H}^+\text{C}_6\text{H}_5\text{NH}_2$ at 1347 (ν_{15}) and 1189 (ν_{17}) cm⁻¹, respectively. Some in-plane and out-of-plane CH -bending modes are predicted to be also intense. For *para*- $\text{H}^+\text{C}_6\text{H}_5\text{NH}_2$, the in-plane CH -bending modes are predicted at 1513 (ν_7) and 1202 (ν_{10}) cm⁻¹, and out-of-plane CH -bending modes at 891 (ν_{22}), 823 (ν_{23}), and 563 (ν_{25}) cm⁻¹; for *ortho*- $\text{H}^+\text{C}_6\text{H}_5\text{NH}_2$, the in-plane CH -bending modes are predicted at 1506 (ν_{11}), 1440 (ν_{12}), and 1415 (ν_{13}) cm⁻¹, and out-of-plane CH -bending modes at 833 (ν_{33}) and 743 (ν_{34}) cm⁻¹; for

amino-H⁺C₆H₅NH₂, the out-of-plane CH-bending modes are predicted at 744 (ν_{34}) and 690 (ν_{35}) cm⁻¹. The corresponding vibrational modes of *meta*- and *ipso*-H⁺C₆H₅NH₂ are also predicted to be intense; see Tables S-4 and S-5.

4. EXPERIMENTAL RESULTS

4A. IR Spectrum of C₆H₅NH₂ in Solid *p*-H₂. Figure 4(a) shows IR spectrum of a C₆H₅NH₂/*p*-H₂ matrix in the spectral range 1700–400 cm⁻¹. Observed line positions and relative intensities are compared with those reported for aniline in solid Ar⁴⁷ in Table S-6; they are in satisfactory agreement. Intense IR lines of C₆H₅NH₂ in solid *p*-H₂ were observed at 3416.2, 3503.6, 3048.4, 1621.4, 1503.4, 1282.8, 754.9, and 690.1 cm⁻¹, with the most intense line at 1621.4 cm⁻¹. Including weaker ones, 24 lines were identified, compared with 15 lines reported for aniline in solid Ar.

The observed vibrational wavenumbers are plotted against the harmonic vibrational wavenumbers predicted with the B3LYP/cc-pVTZ method in Figure S-1. Linear regression analyses yielded satisfactorily linear relations with scaling equations $y = (0.9212 \pm 0.031) x + (138 \pm 101)$ for wavenumbers above 2000 cm⁻¹ and $y = (0.9716 \pm 0.004) x + (8.5 \pm 4.6)$ for wavenumbers less than 2000 cm⁻¹; in these equations, y is the scaled vibrational wavenumber and x is the calculated harmonic vibrational wavenumber. We applied these equations to scale the harmonic vibrational wavenumbers predicted for C₆H₅NH₂ and isomers of H⁺C₆H₅NH₂ to compare with experiment.

The predicted spectrum of C₆H₅NH₂ simulated according to the scaled harmonic vibrational wavenumbers and IR intensities is shown in Figure 4(b) to compare with experiment [Figure 4(a)]. A satisfactory agreement is observed between experimental and predicted spectra in terms of line positions and relative intensities (Table S-6). The line marked with * at 589 cm⁻¹ is predicted for the NH₂-wagging (inversion) mode. As the inversion barrier for the NH₂ group

is small,⁴⁸⁻⁴⁹ this vibrational mode is significantly anharmonic, so that harmonic vibrational analysis predicts poorly its wavenumber and intensity. The fundamental and overtone transitions of this mode were observed at 40.8, 423.8, and 700.1 cm^{-1} in the gaseous phase,⁵⁰⁻⁵² and the overtone transitions were observed at 421, 701 (700), and 1090 (1084.6/1090) cm^{-1} in an Ar matrix,⁴⁹ in which the wavenumbers in parentheses are from Ref. 47. The absence of the inversion mode in solid *p*-H₂ might indicate that this large-amplitude motion is restricted, similar to that in solid N₂.⁴⁹

4B. IR Spectrum of an Electron-Bombarded C₆H₅NH₂/*p*-H₂ Matrix. Figure 5 shows representative IR difference spectra obtained for an electron bombarded C₆H₅NH₂/*p*-H₂ matrix in spectral ranges 3550–3200 and 1560–1150 cm^{-1} ; other regions including 1150–500 cm^{-1} are presented in Figure S-2. Traces in Figure 5(a) present the spectra of aniline C₆H₅NH₂ deposited without electron bombardment and those in Figure 5(b) present the spectra recorded after deposition of electron-bombarded matrix for 10 h, with the lines of C₆H₅NH₂ stripped using Figure 5(a). The positive lines in this spectrum are hence induced by electron bombardment; some parent absorption lines shifted slightly so that they showed a band shape of first-derivative type. Figure 5(c) shows the difference spectrum after maintaining the matrix under darkness for 19 h; lines pointing upward indicate generation and those pointing downward indicate destruction. After this process, the matrix was irradiated at 375 nm for 10 min, followed by irradiation at 254 nm for 30 min. The difference spectra showing the results of these two steps are shown in Figures 5(d) and 5(e), respectively.

The electron bombardment of a *p*-H₂ matrix during deposition is known to produce proton (H₃⁺) and hydrogen atom; proton-transfer and hydrogenation reactions produce protonated and hydrogenated products, respectively.^{27-28, 53} After maintaining the matrix in darkness for a prolonged period, the protonated products become slowly neutralized by originally solvated

electrons to produce their neutral counterparts; the trapped hydrogen atoms might react further with parent molecules to produce hydrogenated products. As a result, we expect that the intensities of lines of protonated species decrease while those for hydrogenated species increase after maintenance of the matrix in darkness for a prolonged period. We identified several groups of lines that decreased during this period and marked them with red circles (group A⁺), green squares (group B⁺), and blue diamonds (group C⁺) in trace (b). The classification of observed lines into three groups was made according to their behavior upon secondary photolysis at 375 and 254 nm. The intensities of lines in group A⁺ decreased upon irradiation at 254 nm (Figure 5(e)) to an extent similar to that observed after maintaining the matrix sample in darkness for 19 h (Figure 5(c)), but ~30 % that observed after deposition (Figure 5(b)). Slightly decreased intensities of lines in group A⁺ were also observed upon irradiation at 375 nm (Figure 5(c)). The intensities of lines in group B⁺ decreased upon irradiation at 375 nm with a proportion similar to that observed after maintaining the matrix sample in darkness for 19 h, but ~20 % that observed after deposition; no further decreased intensity was observed upon irradiation at 254 nm. In contrast, the intensities of lines in group C⁺ remained nearly unchanged upon secondary photolysis at 375 and 254 nm.

Lines in group A⁺ include the intense ones observed at 3482.7, **3395.5**, **1669.2**, and 1523.5 cm⁻¹ and weaker ones at 3289.0(?), 1440.7(?), 1337.2, 1197.5, 884.2, 874.1(?), 816.7, and 561.3 cm⁻¹; the two most intense lines are indicated in bold font and the ? mark indicates that the intensity correlation of the line was less consistent, likely because of interference from other lines. The integrated relative intensities are listed in Table 2. Lines in group B⁺ include intense ones at **3479.3**, 3392.1, 3372.2, 1667.0, and **1515.7** cm⁻¹ and weaker ones at 1541.9, 1452.0, 1419.3, 1341.6, 1188.1, 966.2, 786.1, and 736.1 cm⁻¹ (Table 3). A smaller number of lines at 3303.3, 3278.8, 3234.2, 1470.0, and 737.7 cm⁻¹ are identified to belong to group C⁺ (Table 4).

To be discussed in Sec 5A, lines in groups A⁺, B⁺, and C⁺ are assigned to *para*-, *ortho*-, and *amino*-H⁺C₆H₅NH₂, respectively.

In addition to the lines of which intensities decreased after maintaining the sample in darkness for a prolonged period, we identified several groups of lines of which intensities increased with time; these lines presumably originated from mono-hydrogenated aniline isomers, HC₆H₅NH₂. We shall present the assignments of these species in a separate paper.

5. DISCUSSION

As discussed in Sec. 4B, lines that decreased in intensity after maintenance of the matrix sample in darkness likely correspond to isomers of protonated aniline, H⁺C₆H₅NH₂. We demonstrated that these lines are classified into three groups (A⁺, B⁺, and C⁺) according to their behavior upon secondary photolysis at 375 and 254 nm. In Figure 6, the lines in groups A⁺, B⁺, and C⁺ are compared with spectra predicted for five isomers of H⁺C₆H₅NH₂. The difference spectrum after the secondary photolysis at 254 nm, Figure 5(e), is inverted and presented in Figure 6(a) so that lines in group A⁺ are pointing upward and indicated with red circles. The difference spectrum after the secondary photolysis at 375 nm, Figure 5(c), is inverted and presented in Figure 6(c) so that the lines in group B⁺ are pointing upward and indicated with green squares. The difference spectrum after maintaining the electron-bombarded matrix in darkness for 19 h, Figure 5(b), is inverted and presented in Figure 6(e); lines in group C⁺ are indicated with blue diamonds. Figures 6(b), (d), (f), (g), and (h) present stick IR spectra of *para*-, *ortho*-, *amino*-, *meta*-, and *ipso*-H⁺C₆H₅NH₂, respectively, simulated according to the scaled harmonic vibrational wavenumbers and IR intensities calculated with the B3LYP/cc-pVTZ method.

5A. Assignment of Lines in Groups A⁺ and B⁺ to *para*- and *ortho*-H⁺C₆H₅NH₂. The predicted spectra of *para*- and *ortho*-H⁺C₆H₅NH₂ in the NH-stretching region above 3200 cm⁻¹ are similar; lines of *para*-H⁺C₆H₅NH₂ are predicted at 3510 and 3407 cm⁻¹, slightly blue-shifted from those predicted for *ortho*-H⁺C₆H₅NH₂ at 3508 and 3406 cm⁻¹. Those of *meta*-H⁺C₆H₅NH₂ are further blue-shifted to 3563 and 3459 cm⁻¹, whereas those in *ipso*-H⁺C₆H₅NH₂ are predicted at 3459 and 3380 cm⁻¹. In the experiments, partially overlapped lines were observed to belong to groups A⁺ (3482.7 and 3395.5 cm⁻¹) and B⁺ (3479.3 and 3392.1 cm⁻¹). The observed spectral patterns (wavenumber and intensity) indicate that these lines in groups A⁺ and B⁺ are most likely due to *para*-H⁺C₆H₅NH₂ or *ortho*-H⁺C₆H₅NH₂; the assignment to *meta*-H⁺C₆H₅NH₂ is less likely, but cannot be positively excluded. Because the CH-stretching modes in H⁺C₆H₅NH₂ are predicted to be weak (with IR intensities less than 5 km mol⁻¹) and because of severe interference from absorption of C₆H₅NH₂, we could not positively identify lines of the CH-stretching modes of H⁺C₆H₅NH₂.

The observed and predicted spectra are further compared in the spectral region below 1700 cm⁻¹, in which the predicted spectra of various isomers of H⁺C₆H₅NH₂ are distinct. In this spectral region, lines in group A⁺ were observed at 1669.2, 1523.5, 1440.7 (?), 1337.2, 1197.5, 884.2, 874.1 (?), 816.7, and 561.3 cm⁻¹ (Figure 6(a)), in satisfactory agreement with intense lines of *para*-H⁺C₆H₅NH₂ predicted at 1661, 1513, 1463, 1338, 1202, 891, 882, 823, and 563 cm⁻¹ (Figure 6(b)); the NH₂-inversion mode was predicted at 616 cm⁻¹ but, similarly to the case of aniline, was unobserved. An additional weak line observed at 3289.0 cm⁻¹ is most likely due to the first overtone of the NH₂-scissoring mode (2ν₅), which is predicted at 3307 cm⁻¹ according to the anharmonic vibrational calculation with the B3LYP/cc-pVTZ method. The spectral pattern of these observed 12 lines agrees poorly with those predicted for other isomers of H⁺C₆H₅NH₂; these lines in group A⁺ are thus assigned to *para*-H⁺C₆H₅NH₂. The observed and predicted wavenumbers and relative intensities for *para*-H⁺C₆H₅NH₂ are summarized in

Table 2. The average absolute deviation between experiments and scaled harmonic wavenumbers is $10.0 \pm 8.1 \text{ cm}^{-1}$.

In the spectral region below 1700 cm^{-1} , we observed intense lines in group B⁺ at 1667.0, 1515.7, and 736.1 cm^{-1} , and weaker ones at 1541.9, 1452.0, 1419.3, 1341.6, 1188.1, 966.2, and 786.1 cm^{-1} (Figure 6(c)). This observed spectral pattern agrees satisfactorily with those predicted for *ortho*-H⁺C₆H₅NH₂ with intense lines at 1659, 1506, and 743 cm^{-1} and weaker ones at 1536, 1440, 1415, 1347, 1189, 964, and 774 cm^{-1} (Figure 6(d)); the NH₂-inversion mode was predicted at 595 cm^{-1} but, similarly to the case of aniline, was unobserved. Although we could not distinguish absorption lines of the NH-stretching modes of *para*- and *ortho*-H⁺C₆H₅NH₂ by simple comparison with calculations, we could clearly distinguish these two isomers from the spectral pattern in region $500\text{--}1700 \text{ cm}^{-1}$ and associate them with lines in the NH-stretching region. Our observation of wavenumbers of lines in group B⁺ at 3479.3 and 3392.1 cm^{-1} in the NH-stretching region, slightly red-shifted from those in group A⁺, is consistent with quantum-chemical calculations that predict the wavenumbers of NH-stretching modes of *ortho*-H⁺C₆H₅NH₂ to be slightly smaller than those of *para*-H⁺C₆H₅NH₂. A weak line observed at 3372.2 cm^{-1} appears to be correlated with other lines in group B⁺, but no corresponding line was predicted in anharmonic vibrational calculations. We hence tentatively assign this line to originate from an anharmonic resonance (e.g., Fermi resonance). Based on these comparisons, we assign 13 lines in group B⁺ to *ortho*-H⁺C₆H₅NH₂. The observed and predicted wavenumbers and relative intensities for *ortho*-H⁺C₆H₅NH₂ are summarized in Table 3. The average absolute deviation of $9.0 \pm 7.0 \text{ cm}^{-1}$ for *ortho*-H⁺C₆H₅NH₂ indicates a satisfactory agreement between experimental and scaled harmonic wavenumbers.

5B. Assignment of Lines in Group C⁺ to *amino*-H⁺C₆H₅NH₂. For lines in group C⁺, three intense lines in the NH-stretching region at 3303.3, 3278.8, and 3234.2 cm^{-1} correlate well

with those predicted for *amino*-H⁺C₆H₅NH₂ at 3326, 3311, and 3255 cm⁻¹. In addition to these lines, we identified two lines at 1470.0 and 737.7 cm⁻¹ to belong to group C⁺. These lines agree, in terms of positions and relative intensities, with two intense lines at 1470 and 744 cm⁻¹ predicted for *amino*-H⁺C₆H₅NH₂. Although additional intense lines were predicted at 1638 (v₈) and 1603 (v₉) cm⁻¹ for the NH₂-scissoring modes, respectively, the corresponding lines were not identified because of severe interference from the parent. We assign these five lines in group C⁺ to *amino*-H⁺C₆H₅NH₂. The observed and predicted wavenumbers and relative intensities for *ortho*-H⁺C₆H₅NH₂ are summarized in Table 4. The average absolute deviation is 18.0 ± 13.0 cm⁻¹ for the scaled harmonic wavenumbers. This deviation is slightly greater than those of the other two isomers, presumably because the appropriate scaling factors for the NH-stretching modes might differ slightly for the NH₃ group of *amino*-H⁺C₆H₅NH₂ from those for the NH₂ groups of *para*- and *ortho*-H⁺C₆H₅NH₂. The ultraviolet and visible spectra of various isomers of H⁺C₆H₅NH₂ predicted with time-dependent density functional theory (TD-DFT) support our assignment: see SI text, Figure S-3 and Table S-7.

5C. Comparison with IRPD Spectrum. The IRPD spectra of H⁺C₆H₅NH₂ tagged with Ar or N₂ were reported by Pasker et al.;²⁰ they measured IRPD spectra in the NH-stretching region for several tagged species and provided spectral assignments with the aid of theoretical calculations. The reported IRPD spectrum of Ar-tagged H⁺C₆H₅NH₂ is compared with our IR absorption spectrum of H⁺C₆H₅NH₂ isolated in solid *p*-H₂ and the predicted IR spectrum in Figure 8. The IRPD bands of Ar-H⁺C₆H₅NH₂ (trace a) were reported at 3491, 3402, 3324, 3294, 3242, and 3175 cm⁻¹. The first two bands were assigned to NH-stretching modes of *para*- and/or *ortho*-H⁺C₆H₅NH₂. Because of the expected similar absorption wavenumbers of *para*- and *ortho*-H⁺C₆H₅NH₂ for their NH-stretching modes and the broad bandwidth of IRPD spectra, those authors were unable to distinguish absorption bands of *para*- and *ortho*-H⁺C₆H₅NH₂. In

this work, we successfully resolved the NH-stretching absorption lines at 3482.7 (3479.3) and 3395.5 (3392.1) cm^{-1} of *para*- (*ortho*-) $\text{H}^+\text{C}_6\text{H}_5\text{NH}_2$, as shown in Figure 7(b); numbers in parentheses pertain to the *ortho*-isomer. Our observations agree satisfactorily with quantum-chemical predictions, as discussed in Sec. 5A and shown in Figure 7(c).

The three IRPD bands at 3324, 3294, and 3242 cm^{-1} were assigned to *amino*- $\text{H}^+\text{C}_6\text{H}_5\text{NH}_2$; the most intense band at 3294 cm^{-1} band was assigned to be contributed from *para*-, *ortho*-, and *amino*- $\text{H}^+\text{C}_6\text{H}_5\text{NH}_2$ isomers, as indicated in Figure 7(a). We observed lines at 3303.3, 3278.8, and 3234.2 cm^{-1} attributable to *amino*- $\text{H}^+\text{C}_6\text{H}_5\text{NH}_2$, consistent with the IRPD bands at 3324, 3294, and 3242 cm^{-1} and quantum-chemical predictions at 3336, 3311, and 3255 cm^{-1} . A weak line at 3175 cm^{-1} in the IRPD spectrum was assigned to the first overtone of NH_2 -scissoring mode ($2\nu_8$) of *amino*- $\text{H}^+\text{C}_6\text{H}_5\text{NH}_2$, but the corresponding line was unobserved in solid *p*- H_2 , likely because of its small intensity. The most intense band at 3294 cm^{-1} in the IRPD spectrum is resolved to two lines in our spectrum; according to the behavior on secondary photolysis, the line at 3278.8 cm^{-1} is associated with *amino*- $\text{H}^+\text{C}_6\text{H}_5\text{NH}_2$, but that at 3289.0 cm^{-1} is associated with *para*- $\text{H}^+\text{C}_6\text{H}_5\text{NH}_2$. As discussed above, the latter line might be due to the first overtone of the NH_2 -scissoring mode ($2\nu_5$), which is predicted at 3307 cm^{-1} according to the anharmonic vibrational calculations. We observed an additional line at 3372.2 cm^{-1} to be associated with *ortho*- $\text{H}^+\text{C}_6\text{H}_5\text{NH}_2$. This line was not reported in the IRPD spectrum and might originate from anharmonic resonance, which is affected significantly by the environment (i.e., solid *p*- H_2 vs Ar-tagging).

The wavenumbers of lines in the NH-stretching region observed in solid *p*- H_2 are slightly red-shifted from those observed in the IRPD spectrum. This trend is thought to be due to partial proton sharing between $\text{H}^+\text{C}_6\text{H}_5\text{NH}_2$ and ligands (or matrix). The proton affinities of aniline, Ar and H_2 are 877, 371, and 422 kJ mol^{-1} , respectively,⁵⁴ so the proton-sharing is slightly more enhanced for *p*- H_2 than for Ar as a single ligand. The red shift was slightly larger for *amino*-

$\text{H}^+\text{C}_6\text{H}_5\text{NH}_2$ ($\sim 20 \text{ cm}^{-1}$) compared with that for *para*- $\text{H}^+\text{C}_6\text{H}_5\text{NH}_2$ ($< 10 \text{ cm}^{-1}$). To consider the difference, we calculated the stabilization energy of forming a 1:1 complex between ligand (H_2 or Ar) and $\text{H}^+\text{C}_6\text{H}_5\text{NH}_2$ with the B3LYP/cc-pVTZ method. For *para*- $\text{H}^+\text{C}_6\text{H}_5\text{NH}_2$, complexation of ligand at either the *para*-position or the NH_2 group decrease little the total energy. In contrast, for *amino*- $\text{H}^+\text{C}_6\text{H}_5\text{NH}_2$, complexation of H_2 with the NH_3 group decreases the total energy by 8.4 kJ mol^{-1} , and that of Ar decreases the total energy by 6.4 kJ mol^{-1} , where the energies are uncorrected for the ZPVE and basis set superposition error. These results indicate that a partial proton sharing between $\text{H}^+\text{C}_6\text{H}_5\text{NH}_2$ and ligand is more effective in *amino*- $\text{H}^+\text{C}_6\text{H}_5\text{NH}_2$ and that the complexation with *p*- H_2 induces a larger red shift, consistent with experimental observations.

5D. Mechanism of Formation. In this section, we discuss the mechanism of formation of $\text{H}^+\text{C}_6\text{H}_5\text{NH}_2$ isomers, including proton transfer from H_3^+ to $\text{C}_6\text{H}_5\text{NH}_2$ and possible subsequent rearrangements through tunneling. The mechanism to form $\text{H}^+\text{C}_6\text{H}_5\text{NH}_2$ is expected to be similar to those for the formation of protonated pyridine isomers^{32, 36} and polycyclic aromatic hydrocarbons.^{29-31, 34-35, 55} During *p*- H_2 matrix deposition, H_2 molecules are ionized with electrons to produce H_2^+ ; a subsequent rapid and exothermic proton transfer to a nearby H_2 molecule produces H and H_3^+ . Because the proton affinity of aniline is much greater than that of H_2 , a proton transfer from H_3^+ to aniline occurs readily to produce $\text{H}^+\text{C}_6\text{H}_5\text{NH}_2$: $\text{H}_3^+ + \text{C}_6\text{H}_5\text{NH}_2 \rightarrow \text{H}_2 + \text{H}^+\text{C}_6\text{H}_5\text{NH}_2$. Although spectral evidence for the formation of H_3^+ has yet to be established, the observation of protonated species supports its formation in electron-bombarded *p*- H_2 matrices.

Because the exothermicity of proton transfer reactions ($> 300 \text{ kJ mol}^{-1}$) is significantly greater than the energy barriers separating $\text{H}^+\text{C}_6\text{H}_5\text{NH}_2$ isomers (Figure 3), any isomers can be produced with the proton-transfer reaction except *ipso*- $\text{H}^+\text{C}_6\text{H}_5\text{NH}_2$ that might spontaneously

isomerize to *ortho*-H⁺C₆H₅NH₂. An absence of *meta*-H⁺C₆H₅NH₂ in solid *p*-H₂ might be due to tunneling isomerization to *para*-H⁺C₆H₅NH₂, of which the barrier height is 23 kJ mol⁻¹. The other isomers, *para*-, *ortho*-, and *amino*-H⁺C₆H₅NH₂, are separated from others by sufficiently large (> 100 kJ mol⁻¹) barriers; these isomers are hence stable at low temperatures once stabilized in a solid *p*-H₂ environment.

In contrast with the IRPD method, with which determining the relative abundance of protonated isomers is difficult because several parameters affect the signal intensity, IR absorption spectra in solid *p*-H₂ allow us to estimate the mixing ratios of various isomers according to the method developed by Tam and Fajardo³⁷ (introduced in Sec. 2). Using the integrated intensities of four intense lines in each group and the IR intensities predicted with the B3LYP/cc-pVTZ method, we determined the mixing ratios after matrix deposition to be 1.0 ± 0.1 , 0.6 ± 0.1 , and 1.0 ± 0.6 ppm for *para*-, *ortho*-, and *amino*-H⁺C₆H₅NH₂, respectively; the errors correspond to the standard deviations among mixing ratios estimated from each line. Assuming that the errors in IR intensities of all isomers of H⁺C₆H₅NH₂ predicted with the B3LYP/cc-pVTZ method are similar, we conclude that the two most stable isomers, *para*- and *amino*-H⁺C₆H₅NH₂, were produced in a similar proportion and greater than that of *ortho*-H⁺C₆H₅NH₂, consistent with the expected density of states at the energy of formation. However, more theoretical and experimental investigations are necessary to confirm the model of branching.

6. CONCLUSION

Three isomers of protonated aniline, *para*-, *ortho*-, and *amino*-H⁺C₆H₅NH₂, were produced in an electron-bombarded aniline/*p*-H₂ matrix and characterized with IR spectroscopy. The IR lines of which the intensity decreased during maintenance of the electron-bombarded matrix in darkness were classified into three groups (A⁺, B⁺, and C⁺) according to their behaviors upon

secondary irradiation at 375 and 254 nm. The spectral assignments were made on comparison with the scaled harmonic vibrational wavenumbers and IR intensities predicted with the B3LYP/cc-pVTZ method. Twelve lines in group A⁺, of which the intensity decreased slightly upon irradiation at 375 nm and significantly at 254 nm, were assigned to the most stable *para*-H⁺C₆H₅NH₂. Thirteen lines in group B⁺, of which the intensity decreased significantly upon irradiation at 375 nm but not at 254 nm, were assigned to *ortho*-H⁺C₆H₅NH₂, which is predicted to have greater energy than *para*-H⁺C₆H₅NH₂ by ~18 kJ mol⁻¹. Five lines in group C⁺, which remained unchanged upon secondary photolysis at 375 and 254 nm, were assigned to the second stable *amino*-H⁺C₆H₅NH₂, lying ~8 kJ mol⁻¹ above *para*-H⁺C₆H₅NH₂. The distinct UV-Vis spectra of various isomers of H⁺C₆H₅NH₂, calculated with the TD-CAM-B3LYP/cc-pVTZ method, can explain the behavior of these three isomers upon secondary photolysis. These IR spectra are consistent with the IRPD spectra in the NH-stretching region,²⁰ but lines of *para*- and *ortho*-H⁺C₆H₅NH₂ in this region were clearly resolved in this work. The spectra in region 500–1700 cm⁻¹ are new; they provide definitive identification of *para*- and *ortho*-H⁺C₆H₅NH₂. This identification was enabled through the sufficient spectral resolution and wide spectral coverage available in our method. Through the grouping with lines in the fingerprint region, lines of *para*- and *ortho*-H⁺C₆H₅NH₂ in the NH-stretching region are unambiguously assigned.

The mixing ratios of *para*-, *ortho*-, and *amino*-H⁺C₆H₅NH₂ after matrix deposition were determined to be 1.0 ± 0.1, 0.6 ± 0.1, and 1.0 ± 0.6 ppm, respectively. The observed branching ratios are consistent with the expectation that the more stable isomer has a greater density of states at the energy upon proton transfer.

ASSOCIATED CONTENT

Supporting Information. Full lists of vibrational wavenumbers and IR intensities of *para*-H⁺C₆H₅NH₂ (Table S-1), *ortho*-H⁺C₆H₅NH₂ (Table S-2), *amino*-H⁺C₆H₅NH₂ (Table S-3),

meta-H⁺C₆H₅NH₂ (Table S-4), *ipso*-H⁺C₆H₅NH₂ (Table S-5), and C₆H₅NH₂ (Table S-6). List of vertical excitation energies and oscillator strengths predicted for isomers of H⁺C₆H₅NH₂ (Table S-7). Calibration curves for observed and calculated harmonic vibrational wavenumbers of C₆H₅NH₂. (Figure S-1). Infrared spectra of an electron-bombarded C₆H₅NH₂/*p*-H₂ matrix. (Figure S-2).

AUTHOR INFORMATION

Corresponding Authors

* E-mail (MT): tsuge@lowtem.hokudai.ac.jp.

* E-mail (YPL): yplee@nctu.edu.tw.

Notes

The authors declare no competing financial interest.

ACKNOWLEDGMENT

This work was supported by Ministry of Science and Technology, Taiwan (grants MOST MOST108-2639-M-009-001-ASP and MOST108-3017-F009-004) and the Center for Emergent Functional Matter Science of National Chiao Tung University from The Featured Areas Research Center Program within the framework of the Higher Education Sprout Project by the Ministry of Education (MOE) in Taiwan. The National Center for High-Performance Computation provided computer time. Japan Society for the Promotion of Science (JSPS KAKENHI grant No. JP18K03717) partially supported this work. The National Center for High-Performance Computation of Taiwan and the Information Initiative Center of Hokkaido University are thanked for providing computational resources.

REFERENCES

1. Bell, R. P., *The Proton in Chemistry*. 2 ed.; Cornell University Press: Ithaca, 1973.
2. Hoaglund-Hyzer, C. S.; Counterman, A. E.; Clemmer, D. E., Anhydrous Protein Ions. *Chem. Rev.* **1999**, *99*, 3037–3080.
3. Bagno, A.; Scorrano, G., Selectivity in Proton Transfer, Hydrogen Bonding, and Solvation. *Acc. Chem. Res.* **2000**, *33*, 609–616.
4. Fornarini, S.; Crestoni, M. E., Gaseous Arenium Ions at Atmospheric Pressure: Elementary Reactions and Internal Solvation Effects. *Acc. Chem. Res.* **1998**, *31*, 827–834.
5. Olah, G. A., Aromatic Substitution. XXVIII. Mechanism of Electrophilic Aromatic Substitutions. *Acc. Chem. Res.* **1971**, *4*, 240–248.
6. Lenoir, D., The Electrophilic Substitution of Arenes: Is the π Complex a Key Intermediate and What is Its Nature? *Angew. Chem. Int. Ed.* **2003**, *42*, 854–857.
7. Smith, M. B.; March, J., *Advanced Organic Chemistry: Reactions, Mechanisms, and Structure*. 5th ed.; Wiley: New York, 2001.
8. Bagno, A.; Terrier, F., Carbon and Nitrogen Basicity of Aminothiophenes and Anilines. *J. Phys. Chem. A* **2001**, *105*, 6537–6542.
9. Lau, Y. K.; Kebarle, P., Substituent Effects on the Intrinsic Basicity of Benzene: Proton Affinities of Substituted Benzenes. *J. Am. Chem. Soc.* **1976**, *98*, 7452–7453.
10. Pollack, S. K.; Devlin, J. L.; Summerhays, K. D.; Taft, R. W.; Hehre, W. J., The Site of Protonation in Aniline. *J. Am. Chem. Soc.* **1977**, *99*, 4583–4584.
11. Dewar, M. J. S.; Dieter, K. M., Evaluation of AM1 Calculated Proton Affinities and Deprotonation Enthalpies. *J. Am. Chem. Soc.* **1986**, *108*, 8075–8086.
12. Pachuta, S. J.; Isern-Flecha, I.; Cooks, R. G., Charge Stripping and the Site of Cationization of Substituted Aromatic Compounds. *Org. Mass Spectrom.* **1986**, *21*, 1–5.
13. Karpas, Z.; Berant, Z.; Stimac, R. M., An Ion Mobility Spectrometry/Mass Spectrometry (IMS/MS) Study of the Site of Protonation in Anilines. *Struct. Chem.* **1990**, *1*, 201–204.
14. Smith, R. L.; Chyall, L. J.; Beasley, B. J.; Kenttamaa, H. I., The Site of Protonation of Aniline. *J. Am. Chem. Soc.* **1995**, *117*, 7971–7973.
15. Nold, M. J.; Wesdemiotis, C., Differentiation of N⁻ from C⁻Protonated Aniline by Neutralization–Reionization. *J. Mass Spectrom.* **1996**, *31*, 1169–1172.
16. Hillebrand, C.; Klessinger, M.; Eckert-Maksić, M.; Maksić, Z. B., Theoretical Model Calculations of the Proton Affinities of Aminoalkanes, Aniline, and Pyridine. *J. Phys. Chem.* **1996**, *100*, 9698–9702.

17. Roy, R. K.; de Proft, F.; Geerlings, P., Site of Protonation in Aniline and Substituted Anilines in the Gas Phase: A Study via the Local Hard and Soft Acids and Bases Concept. *J. Phys. Chem. A* **1998**, *102*, 7035–7040.
18. Russo, N.; Toscano, M.; Grand, A.; Mineva, T., Proton Affinity and Protonation Sites of Aniline. Energetic Behavior and Density Functional Reactivity Indices. *J. Phys. Chem. A* **2000**, *104*, 4017–4021.
19. Flammang, R.; Dechamps, N.; Pascal, L.; Vvan Haverbeke, Y.; Gerbaux, P.; Nam, P.-C.; Nguyen, M. T., Ring Versus Nitrogen Protonation of Anilines. *Lett. Org. Chem.* **2004**, *1*, 23–30.
20. Pasker, F. M.; Solcà, N.; Dopfer, O., Spectroscopic Identification of Carbenium and Ammonium Isomers of Protonated Aniline (AnH^+): IR Spectra of Weakly Bound AnH^+-Ln Clusters ($\text{L} = \text{Ar}, \text{N}_2$). *J. Phys. Chem. A* **2006**, *110*, 12793–12804.
21. Lalli, P. M.; Iglesias, B. A.; Toma, H. E.; de Sa, G. F.; Daroda, R. J.; Silva Filho, J. C.; Szulejko, J. E.; Araki, K.; Eberlin, M. N., Protomers: Formation, Separation and Characterization via Travelling Wave Ion Mobility Mass Spectrometry. *J. Mass Spectrom.* **2012**, *47*, 712–719.
22. Attygalle, A. B.; Xia, H.; Pavlov, J., Influence of Ionization Source Conditions on the Gas-Phase Protomer Distribution of Anilinium and Related Cations. *J. Am. Soc. Mass. Spectrom.* **2017**, *28*, 1575–1586.
23. Walker, S. W. C.; Mark, A.; Verbuyst, B.; Bogdanov, B.; Campbell, J. L.; Hopkins, W. S., Characterizing the Tautomers of Protonated Aniline Using Differential Mobility Spectrometry and Mass Spectrometry. *J. Phys. Chem. A* **2018**, *122*, 3858–3865.
24. Lias, S. G.; Bartmess, J. E.; Holmes, J. L.; Levine, R. D.; Mallard, W. G., Gas-Phase Ion and Neutral Thermochemistry. *J. Phys. Chem. Ref. Data* **1988**, *17*, Supplement No. 1.
25. Taft, R. W., Gas-Phase Proton-Transfer Equilibria. In *Proton Transfer Reactions*, Caldin, E. F.; Gold, V., Eds. Wiley-Halstead: New York, 1975.
26. Wood, K. V.; Burinsky, D. J.; Cameron, D.; Cooks, R. G., Site of Gas-phase Cation Attachment. Protonation, Methylation, and Ethylation of Aniline, Phenol, and Thiophenol. *J. Org. Chem.* **1983**, *48*, 5236–5242.
27. Bahou, M.; Das, P.; Lee, Y.-F.; Wu, Y.-J.; Lee, Y.-P., Infrared Spectra of Free Radicals and Protonated Species Produced in *para*-Hydrogen Matrices. *Phys. Chem. Chem. Phys.* **2014**, *16*, 2200–2210.
28. Tsuge, M.; Tseng, C.-Y.; Lee, Y.-P., Spectroscopy of Prospective Interstellar Ions and Radicals Isolated in *para*-Hydrogen Matrices. *Phys. Chem. Chem. Phys.* **2018**, *20*, 5344–5358.

29. Bahou, M.; Wu, Y.-J.; Lee, Y.-P., A New Method for Investigating Infrared Spectra of Protonated Benzene ($C_6H_7^+$) and Cyclohexadienyl Radical ($c-C_6H_7$) Using *para*-Hydrogen. *J. Chem. Phys.* **2012**, *136*, 154304.
30. Bahou, M.; Wu, Y.-J.; Lee, Y.-P., Formation and Infrared Absorption of Protonated Naphthalenes ($1-C_{10}H_9^+$ and $2-C_{10}H_9^+$) and their Neutral Counterparts in Solid *para*-Hydrogen. *Phys. Chem. Chem. Phys.* **2013**, *15*, 1907–1917.
31. Bahou, M.; Wu, Y.-J.; Lee, Y.-P., Infrared Spectra of Protonated Pyrene and its Neutral Counterpart in Solid *para*-Hydrogen. *J. Phys. Chem. Lett.* **2013**, *4*, 1989–1993.
32. Golec, B.; Das, P.; Bahou, M.; Lee, Y.-P., Infrared Spectra of the 1-Pyridinium ($C_5H_5NH^+$) Cation and Pyridinyl (C_5H_5NH and $4-C_5H_6N$) Radicals Isolated in Solid *para*-Hydrogen. *J. Phys. Chem. A* **2013**, *117*, 13680–13690.
33. Bahou, M.; Wu, Y.-J.; Lee, Y.-P., Infrared Spectra of Protonated Coronene and its Neutral Counterpart in Solid Parahydrogen: Implications for Unidentified Interstellar Infrared Emission Bands. *Angew. Chem. Int. Ed.* **2014**, *53*, 1021–1024.
34. Tsuge, M.; Bahou, M.; Wu, Y.-J.; Allamandola, L. J.; Lee, Y.-P., The Infrared Spectrum of Protonated Ovalene in Solid *para*-Hydrogen and its Possible Contribution to Interstellar Unidentified Infrared Emission. *Astrophys. J.* **2016**, *825*, 96.
35. Sundararajan, P.; Tsuge, M.; Baba, M.; Lee, Y.-P., Infrared Spectrum of Protonated Corannulene $H^+C_{20}H_{10}$ in Solid *para*-Hydrogen and its Potential Contribution to Interstellar Unidentified Infrared Bands. *ACS Earth Space Chem.* **2018**, *2*, 1001–1010.
36. Tsuge, M.; Lai, C.-P.; Lee, Y.-P., Infrared Spectra of 3-hydroxy-(1H)-pyridinium Cation and 3-hydroxy-(1H)-pyridinyl Radical Isolated in Solid *para*-Hydrogen. *J. Chem. Phys.* **2018**, *149*, 014306.
37. Tam, S.; Fajardo, M. E., Single and Double Infrared Transitions in Rapid-Vapor-Deposited Parahydrogen Solids: Application to Sample Thickness Determination and Quantitative Infrared Absorption Spectroscopy. *Appl. Spectrosc.* **2001**, *55*, 1634–1644.
38. Ruzi, M.; Anderson, D. T., Photodissociation of N-methylformamide Isolated in Solid Parahydrogen. *J. Chem. Phys.* **2012**, *137*, 194313.
39. Fajardo, M. E., Solid Parahydrogen Thickness Revisited. *Appl. Spectrosc.* **2019**, *73*, 1403–1408.
40. Fajardo, M. E., Matrix Isolation Spectroscopy in Solid Parahydrogen: A Primer. In *Physics and Chemistry at Low Temperatures*, Khriachtchev, L., Ed. Pan Stanford Publishing Pte. Ltd.: Singapore, 2011; pp 167–202.

41. Frisch, M. J.; Trucks, G. W.; Schlegel, H. B.; Scuseria, G. E.; Robb, M. A.; Cheeseman, J. R.; Scalmani, G.; Barone, V.; Mennucci, B.; Petersson, G. A.; et al. *Gaussian 09 Rev. E.01*, Wallingford CT, 2009.
42. Frisch, M. J.; Trucks, G. W.; Schlegel, H. B.; Scuseria, G. E.; Robb, M. A.; Cheeseman, J. R.; Scalmani, G.; Barone, V.; Petersson, G. A.; Nakatsuji, H.; et al. *Gaussian 16 Rev. B.01*, Wallingford, CT, 2016.
43. Becke, A. D., Density-functional Thermochemistry. III. the Role of Exact Exchange. *J. Chem. Phys.* **1993**, *98*, 5648–5652.
44. Lee, C. T.; Yang, W. T.; Parr, R. G., Development of the Colle-Salvetti Correlation-energy Formula into a Functional of the Electron-density. *Phys. Rev. B* **1988**, *37*, 785–789.
45. Dunning Jr., T. H., Gaussian-basis Sets for Use in Correlated Molecular Calculations. 1. The Atoms Boron through Neon and Hydrogen. *J. Chem. Phys.* **1989**, *90*, 1007–1023.
46. Bloino, J.; Barone, V., A second-order perturbation theory route to vibrational averages and transition properties of molecules: general formulation and application to infrared and vibrational circular dichroism spectroscopies. *J. Chem. Phys.* **2012**, *136*, 124108.
47. Gée, C.; Douin, S.; Crépin, C.; Bréchnignac, P., Infrared Spectroscopy of Aniline ($C_6H_5NH_2$) and its Cation in a Cryogenic Argon Matrix. *Chem. Phys. Lett.* **2001**, *338*, 130–136.
48. López-Tocón, I.; Della Valle, R. G.; Becucci, M.; Castellucci, E.; Otero, J. C., NH_2 Inversion Potential in the S_0 and S_1 Electronic States of Aniline: Fit to the (ro-)Vibrational Data and Comparison with ab initio and Density Functional Results. *Chem. Phys. Lett.* **2000**, *327*, 45–53.
49. Mukherjee, M.; Bandyopadhyay, B.; Biswas, P.; Chakraborty, T., Amine Inversion Effects on the IR Spectra of Aniline in the Gas Phase and Cold Inert Gas Matrixes. *Indian J. Phys.* **2012**, *86*, 201–208.
50. Piest, H.; Helden, G. v.; Meijer, G., Infrared Spectroscopy of Jet-cooled Neutral and Ionized Aniline–Ar. *J. Chem. Phys.* **1999**, *110*, 2010–2015.
51. Quack, M.; Stockburger, M., Resonance Fluorescence of Aniline Vapour. *J. Mol. Spectrosc.* **1972**, *43*, 87–116.
52. Kydd, R. A.; Krueger, P. J., The Far-infrared Vapour Phase Spectra of Aniline- ND_2 and Aniline-NHD. *Chem. Phys. Lett.* **1977**, *49*, 539–543.
53. Chan, M.-C.; Okumura, M.; Oka, T., Infrared Spectrum of *p*-Hydrogen Crystals Ionized by 3 MeV Electrons: Cluster Ions of Hydrogen in Condensed Phase. *J. Phys. Chem. A* **2000**, *104*, 3775–3779.

54. Hunter, E. P. L.; Lias, S. G., Evaluated Gas Phase Basicities and Proton Affinities of Molecules: An Update. *J. Phys. Chem. Ref. Data* **1998**, *27*, 413–656.
55. Chakraborty, A.; Lee, Y.-P., Formation and Infrared Identification of Protonated Fluoranthene Isomers 3-, 9-, and 10-C₁₆H₁₁⁺ in Solid *para*-H₂. *Phys. Chem. Chem. Phys.* **2019**, *21*, 1820–1829.

Table 1. Relative Energies (in kJ mol^{-1}) of Isomers of Protonated Aniline and Transition States (TSs) for Isomerization Calculated with the B3LYP Method.

| isomer ^a | relative energy / kJ mol^{-1} | | | |
|---------------------|--|------------------------------|------------------------------|--------------|
| | this work | | literature ^b | |
| | cc-pVTZ ^d | 6-311G(2df,2pd) ^d | 6-311G(2df,2pd) ^d | |
| | | | | ΔE^c |
| <i>para</i> - | 0.0 | 0.0 | 8 | -474.3 |
| <i>amino</i> - | 7.8 | 7.4 | 0 | -466.5 |
| <i>ortho</i> - | 18.4 | 18.3 | 26 | -455.9 |
| <i>meta</i> - | 96.0 | 97.1 | 90 | -378.3 |
| <i>ipso</i> - | 168.3 | 169.9 | 157 | -305.9 |
| TS1 | 119.2 | | 113 | |
| TS2 | 128.4 | | 122 | |
| TS3 | 163.6 | | 155 | |
| TS4 | 236.8 | | 230 | |

^aSee Figure 1 for protonation sites. ^bThe values in parentheses are from Ref. 20: calculated with the B3LYP/6-311G(2df,2pd) method and corrected for ZPVE. ^cEnergy changes in reactions $\text{C}_6\text{H}_5\text{NH}_2 + \text{H}_3^+ \rightarrow \text{H}^+\text{C}_6\text{H}_5\text{NH}_2 + \text{H}_2$ calculated with the B3LYP/cc-pVTZ method. ^dBasis set.

Table 2. Comparison of Experimental Vibrational Wavenumbers (cm^{-1}) and Relative IR Intensities of *para*- $\text{H}^+\text{C}_6\text{H}_5\text{NH}_2$ (Lines in group A⁺) with Corresponding Values Predicted with the B3LYP/cc-pVTZ Method.^a

| mode (sym.) | calculated ^b | <i>p</i> -H ₂ | IRPD ^c |
|----------------------|-------------------------|--------------------------|-------------------|
| ν_{28} (b_2) | 3510 (20) ^d | 3482.7 (17) ^e | 3491 |
| ν_1 (a_1) | 3407 (53) | 3395.5 (53) | 3402 |
| $2\nu_5$ (a_1) | 3307 (<1) ^f | 3289.0 (10) ^g | 3294 |
| ν_5 (a_1) | 1661 (100) | 1669.2 (100) | |
| ν_7 (a_1) | 1513 (19) | 1523.5 (20) | |
| ν_{32} (b_2) | 1463 (13) | 1440.7 (7) ^g | |
| ν_{34} (b_2) | 1338 (19) | 1337.2 (12) | |
| ν_{10} (a_1) | 1202 (10) | 1197.5 (9) | |
| ν_{22} (b_1) | 891 (8) | 884.2 (8) | |
| ν_{12} (a_1) | 882 (17) | 874.1 (9) ^g | |
| ν_{23} (b_1) | 823 (6) | 816.7 (12) | |
| ν_{25} (b_1) | 563 (20) | 561.3 (12) | |

^aTable S-1 presents a list of all vibrational modes. ^bScaled harmonic vibrational wavenumbers; see text. ^cAr-tagged *para*- (and/or *ortho*-) $\text{H}^+\text{C}_6\text{H}_5\text{NH}_2$, from Ref. 20. ^dThe predicted IR intensities shown in parentheses are normalized to the intensity of the most intense line (ν_5), 432 km mol^{-1} . ^eIntegrated IR intensities as a percentage of the most intense line at 1669.2 cm^{-1} (ν_5) are shown in parentheses. ^fWavenumber and IR intensity calculated with the anharmonic VPT2 calculation. ^gAssignments are tentative.

Table 3. Comparison of Experimental Vibrational Wavenumbers (cm^{-1}) and Relative IR Intensities of *ortho*- $\text{H}^+\text{C}_6\text{H}_5\text{NH}_2$ (lines in group B⁺) with Corresponding Values Predicted with the B3LYP/cc-pVTZ Method.^a

| mode (sym.) | calculated ^b | <i>p</i> -H ₂ | IRPD ^c |
|---------------------------|-------------------------|---------------------------|-------------------|
| ν_1 (<i>a'</i>) | 3508 (28) ^d | 3479.3 (120) ^e | 3491 |
| ν_2 (<i>a'</i>) | 3406 (77) | 3392.1 (81) | 3402 |
| ν_f | – | 3372.2 (40) | 3294 |
| ν_8 (<i>a'</i>) | 1660 (89) | 1667.0 (72) | |
| ν_{10} (<i>a'</i>) | 1536 (13) | 1541.9 (19) | |
| ν_{11} (<i>a'</i>) | 1506 (100) | 1515.7 (100) | |
| ν_{12} (<i>a'</i>) | 1440 (9) | 1452.0 (24) | |
| ν_{13} (<i>a'</i>) | 1415 (16) | 1419.3 (15) | |
| ν_{15} (<i>a'</i>) | 1347 (12) | 1341.6 (25) | |
| ν_{17} (<i>a'</i>) | 1189 (12) | 1188.1 (19) | |
| ν_{21} (<i>a'</i>) | 964 (12) | 966.2 (9) | |
| ν_{23} (<i>a'</i>) | 774 (2) | 786.1 (11) | |
| ν_{34} (<i>a''</i>) | 743 (16) | 736.1 (65) | |

^aTable S-2 presents a list of all vibrational modes. ^bScaled harmonic vibrational wavenumbers; see text. ^cAr-tagged *para*- (and/or *ortho*-) $\text{H}^+\text{C}_6\text{H}_5\text{NH}_2$, from Ref. 20. ^dThe predicted IR intensities shown in parentheses are normalized to the most intense line (ν_{11}), 260 km mol^{-1} . ^eIntegrated IR intensities as a percentage of the intense line at 1515.7 cm^{-1} (ν_{11}) are shown in parentheses. ^fThis observed line might be due to anharmonic resonance, because the anharmonic VPT2 calculation predicts no line nearby.

Table 4. Comparison of Experimental Vibrational Wavenumbers (cm^{-1}) and Relative IR Intensities of *amino*- $\text{H}^+\text{C}_6\text{H}_5\text{NH}_2$ (lines in group C^+) with Corresponding Values Predicted with the B3LYP/cc-pVTZ Method.^a

| mode (sym.) | calculated ^b | <i>p</i> -H ₂ | IRPD ^c |
|---------------------------|-------------------------|--------------------------|-------------------|
| ν_1 (<i>a'</i>) | 3336 (71) ^d | 3303.3 (75) ^e | 3324 |
| ν_{27} (<i>a''</i>) | 3311 (91) | 3278.8 (90) | 3294 |
| ν_2 (<i>a'</i>) | 3255 (48) | 3234.2 (40) | 3242 |
| ν_{13} (<i>a'</i>) | 1470 (100) | 1470.0 (100) | |
| ν_{34} (<i>a''</i>) | 744 (49) | 737.7 (50) | |

^aTable S-3 presents a list of all vibrational modes. ^bScaled harmonic vibrational wavenumbers; see text. ^cAr-tagged *amino*- $\text{H}^+\text{C}_6\text{H}_5\text{NH}_2$, from Ref. 20. ^dThe predicted IR intensities shown in parentheses are normalized to the intensity of the most intense line (ν_{13}), 116 km mol^{-1} . ^eIntegrated IR intensities as a percentage of the most intense line at 1470.0 cm^{-1} (ν_{13}) are shown in parentheses.

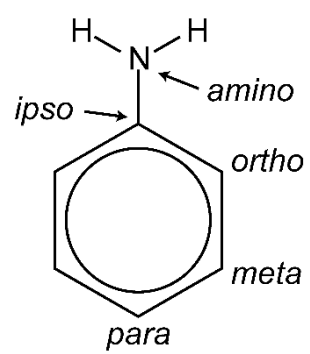


Figure 1. Five distinct protonation sites in aniline (C₆H₅NH₂).

(single column)

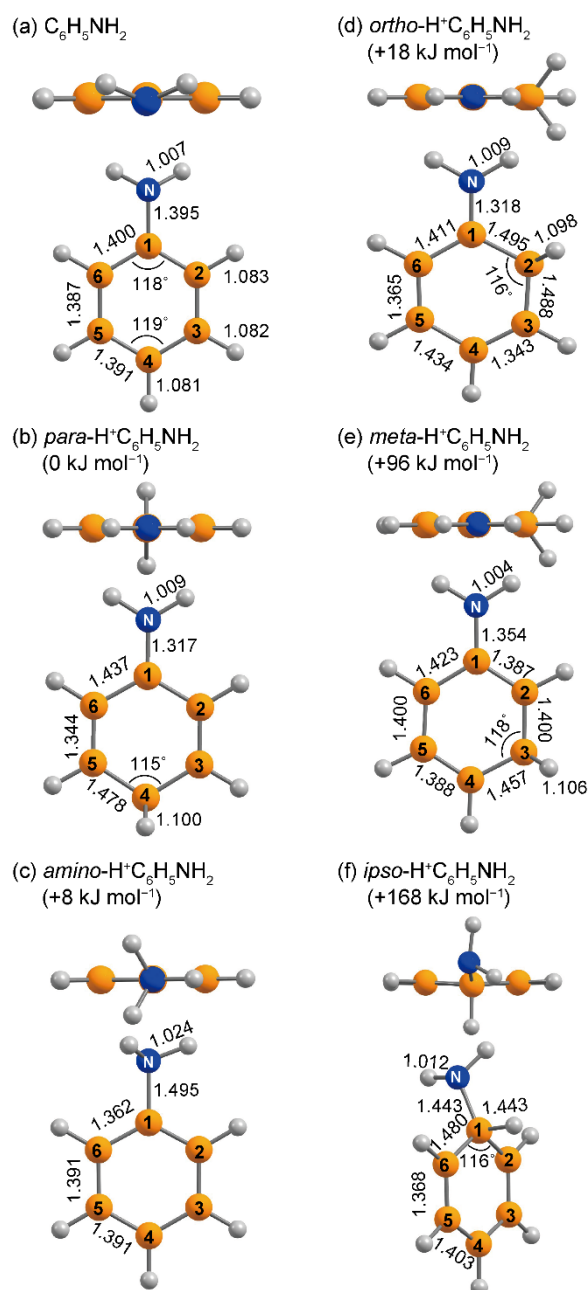


Figure 2. Geometries of (a) $\text{C}_6\text{H}_5\text{NH}_2$, (b) *para*- $\text{H}^+\text{C}_6\text{H}_5\text{NH}_2$, (c) *amino*- $\text{H}^+\text{C}_6\text{H}_5\text{NH}_2$, (d) *ortho*- $\text{H}^+\text{C}_6\text{H}_5\text{NH}_2$, (e) *meta*- $\text{H}^+\text{C}_6\text{H}_5\text{NH}_2$, and (f) *ipso*- $\text{H}^+\text{C}_6\text{H}_5\text{NH}_2$ optimized with the B3LYP/cc-pVTZ method. The bottom figure in (f) is tilted so that the *ipso*-position is visible. For $\text{H}^+\text{C}_6\text{H}_5\text{NH}_2$ isomers, the ZPVE-corrected relative energies are shown in parentheses. Bond lengths are in Å.

(single column)

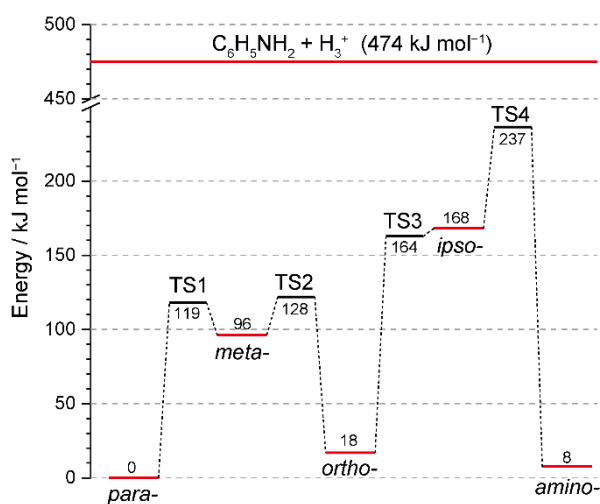


Figure 3. Calculated relative energies of isomers of protonated aniline (*para*-, *meta*-, *ortho*-, *ipso*-, and *amino*- $\text{H}^+\text{C}_6\text{H}_5\text{NH}_2$) and transition states (TS) connecting them. Calculations were performed with the B3LYP/cc-pVTZ method; zero-point vibrational energies were corrected with unscaled harmonic vibrational energies. The energy level of $\text{H}^+\text{C}_6\text{H}_5\text{NH}_2 + \text{H}_2$ are relative to the most stable "*para*- $\text{H}^+\text{C}_6\text{H}_5\text{NH}_2 + \text{H}_2$ " pair.

(single column)

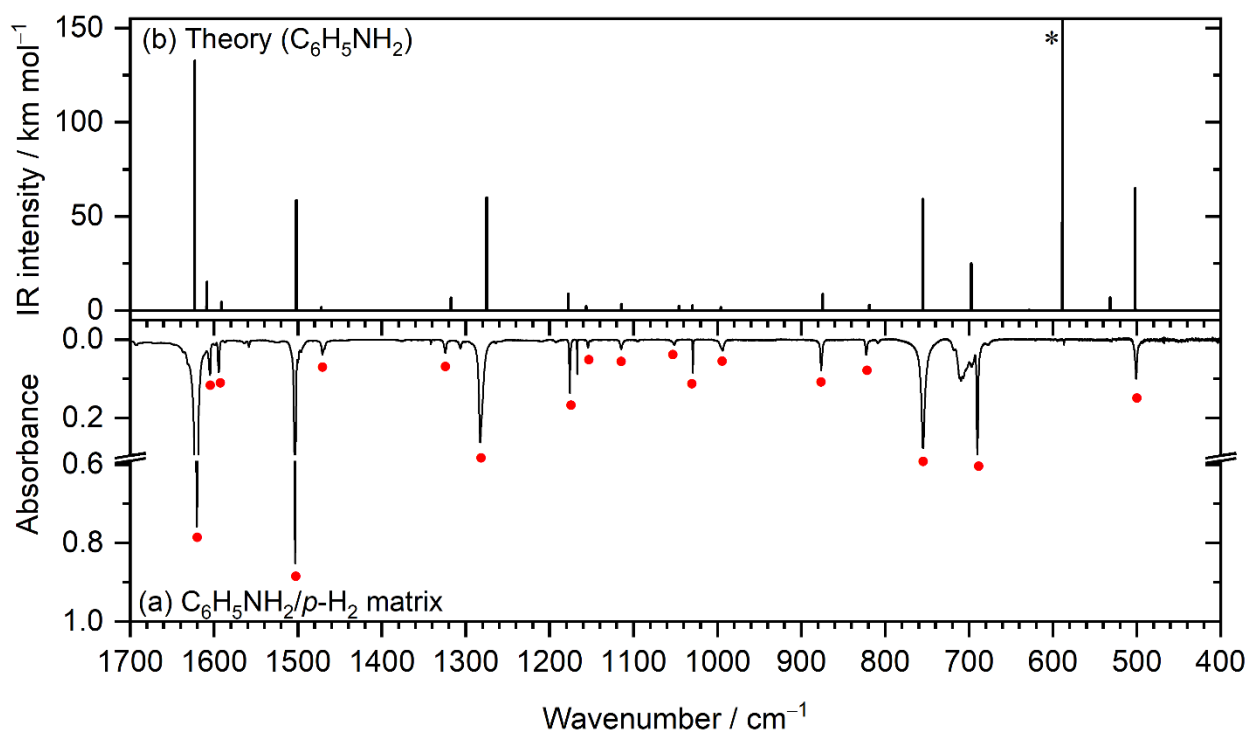


Figure 4. Comparison of experimental and predicted IR spectra of C₆H₅NH₂. (a) Experimental absorption spectrum in solid *p*-H₂; red dots indicate the lines assigned to C₆H₅NH₂. (b) Simulated stick spectrum of C₆H₅NH₂ according to scaled harmonic vibrational wavenumbers and IR intensities predicted with the B3LYP/cc-pVTZ method. The line marked with * is due to the NH₂ wagging (inversion) mode, which cannot be predicted properly with the harmonic vibrational analysis; see text. The observed and predicted wavenumbers and IR intensities are listed in Table S-6.

(double column)

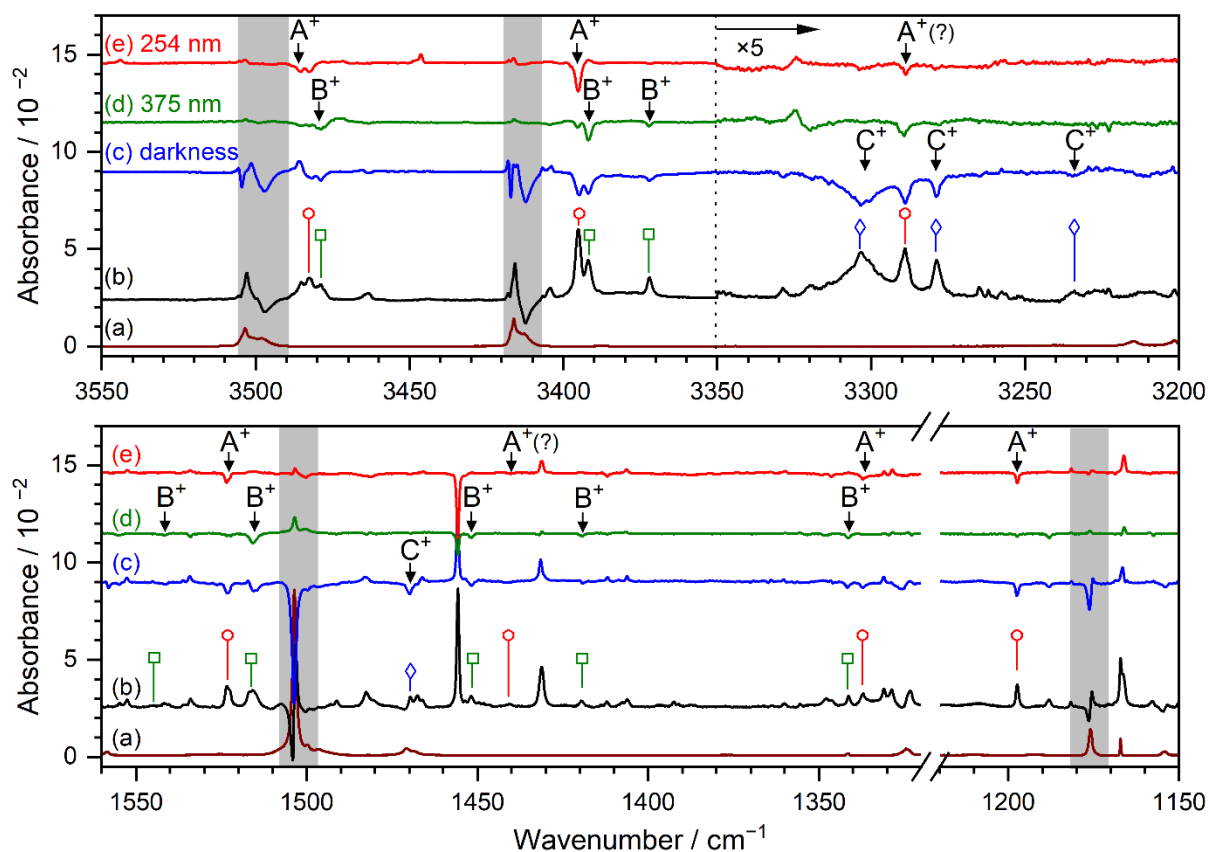


Figure 5. Representative infrared spectra of an electron-bombarded $C_6H_5NH_2/p-H_2$ matrix in spectral regions 3550–3200 and 1560–1150 cm^{-1} . (a) IR spectrum of $C_6H_5NH_2$. (b) IR spectrum of an electron-bombarded $C_6H_5NH_2/p-H_2$ matrix recorded after matrix deposition for 10 h; the lines of $C_6H_5NH_2$ are stripped according to (a). (c) Difference spectrum of the matrix after maintenance in darkness for 19 h. (d) Difference spectrum after secondary photolysis at 375 nm for 10 min. (e) Difference spectrum after further secondary photolysis at 254 nm for 30 min. In the difference spectra, lines pointing upward indicate generation and those pointing downward indicate destruction. The lines in groups A^+ , B^+ , and C^+ are indicated with red circles, green squares, and blue diamonds, respectively. The regions suffering from interference are indicated with gray rectangles.

(double column)

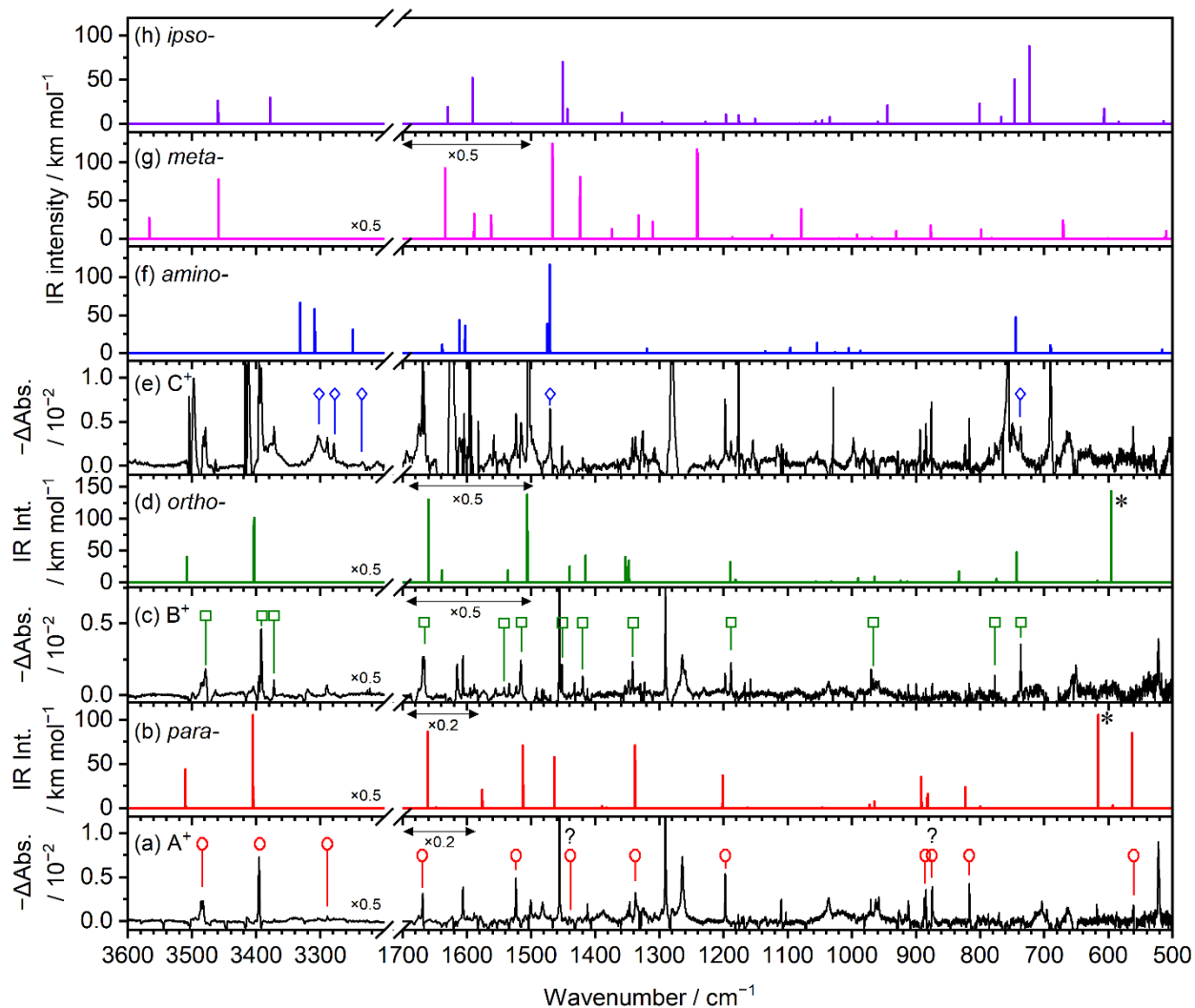


Figure 6. Comparison of experimental and predicted IR spectra of various isomers of $\text{H}^+\text{C}_6\text{H}_5\text{NH}_2$. (a) Difference spectrum after secondary photolysis at 254 nm for 30 min; inverted Figure 5(e). The lines in group A^+ are indicated with red circles. (b) Predicted IR spectrum of *para*- $\text{H}^+\text{C}_6\text{H}_5\text{NH}_2$. (c) Difference spectrum after secondary photolysis at 375 nm for 10 min; inverted Figure 5(d). The lines in group B^+ are indicated with green squares. (d) Predicted IR spectrum of *ortho*- $\text{H}^+\text{C}_6\text{H}_5\text{NH}_2$. (e) Difference spectrum after maintaining the matrix in darkness for 19 h; inverted Figure 5(b). The lines in group C^+ are indicated with blue diamonds. (f) Predicted infrared spectrum of *amino*- $\text{H}^+\text{C}_6\text{H}_5\text{NH}_2$. (g) Predicted IR spectrum of *meta*- $\text{H}^+\text{C}_6\text{H}_5\text{NH}_2$. (h) Predicted IR spectrum of *ipso*- $\text{H}^+\text{C}_6\text{H}_5\text{NH}_2$. Predicted spectra were simulated according to scaled harmonic vibrational wavenumbers and IR intensities calculated with the B3LYP/cc-pVTZ method. Predicted lines marked with * are due to the NH_2 -wagging (inversion) modes, which cannot be predicted properly with the harmonic vibrational analysis. (double column)

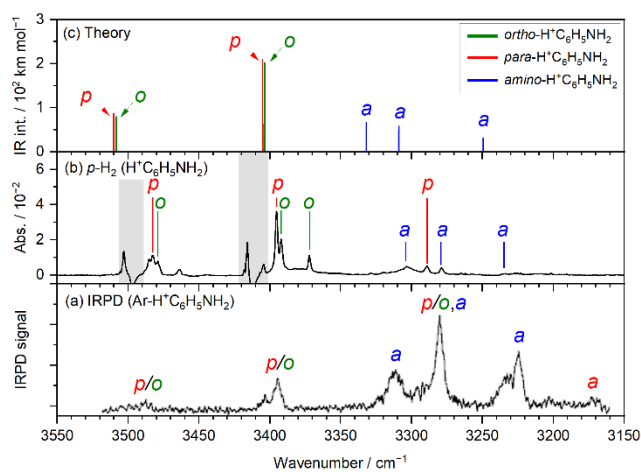
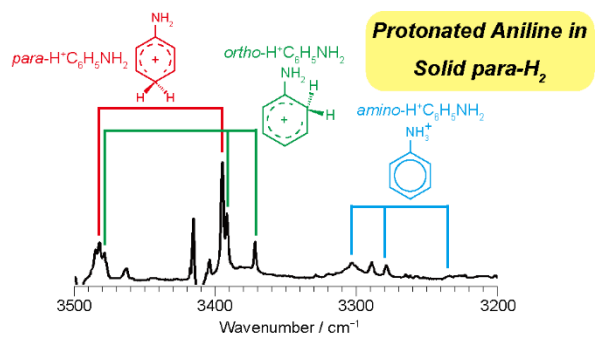


Figure 7. Comparison of IR spectra in the NH-stretching region. (a) IR photodissociation (IRPD) spectrum of Ar-tagged H⁺C₆H₅NH₂; taken from Ref. 20. (b) IR absorption spectrum of an electron-bombarded C₆H₅NH₂/p-H₂ matrix; taken from Figure 5(b). (c) Stick spectrum according to scaled harmonic vibrational calculations with the B3LYP/cc-pVTZ method. The lines assigned to *para*-, *ortho*-, and *amino*-H⁺C₆H₅NH₂ are indicated with *p*, *o*, and *a*, respectively.

(single column)



TOC Graphic